Hydrous ringwoodite to 5 K and 35 GPa:

Multiple hydrogen bonding sites resolved with FTIR spectroscopy

Revision 3

Wendy R. Panero[1] Joseph R. Smyth[2], Jeffrey S. Pigott[1], Zhenxian Liu[3], and Daniel J. Frost[4]

[1]School of Earth Sciences, Ohio State University, Columbus, OH 43210

[2]Department of Geological Sciences, University of Colorado, Boulder, CO 80309

[3]Geophysical Laboratory, Carnegie Institution of Washington, Washington D.C. 20015

[4]Bayerisches Geoinstitut, Universität Bayreuth, Bayreuth D95440, Germany

Abstract

Multiple substitution mechanisms for hydrogen in γ-$(Mg,Fe)_2SiO_4$, ringwoodite, lead to broad, overlapping and difficult-to-interpret FTIR spectra. Through combined low-temperature, high-pressure synchrotron-based FTIR spectroscopy, the multiple bonding sites become evident, and can be traced as a function of temperature and compression. Multiple OH stretching bands can be resolved in iron-bearing and iron-free samples with 0.79-2.5(3) wt% H_2O below 200 K at ambient pressure, with cooling to 5K at 35 GPa and 23 GPa resulting in the resolution of possibly as many as 5 OH stretching bands traceable at room temperature from 23 GPa down to 8 GPa. A distribution of defect mechanisms between $V_{Mg}^{''}$+2($H^{\bullet}$) at 3100 cm^{-1}, 3270 cm^{-1}, and possibly 2654 cm^{-1}, $V_{Si}^{''''}$+4($H^{\bullet}$) at 3640 cm^{-1}, and $Mg_{Si}^{''}$+2($H^{\bullet}$) at 2800 cm^{-1} can then be resolved. These multiple defect mechanisms can therefore explain the higher electrical and proton conductivity in

ringwoodite when compared to wadsleyite, and therefore may be applied to resolve spatial variations in water storage in the Earth's transition zone.

Keywords: Ringwoodite, FTIR, low temperature

Introduction

The transition zone has a water storage capacity of 1-2 wt% H_2O (e.g., Kohlstedt et al. 1996; Bolfan-Casanova et al. 2000; Ohtani et al. 2000; Demouchy et al. 2005) where, in the absence of excess water and associated fluids or melt, considerable OH can be found in the crystal structures of major minerals of the pyrolite assemblage at that depth. The major carriers of water in the transition zone are the olivine polymorphs, wadsleyite, and ringwoodite. The hydrogen content in the olivine polymorphs affects a variety of physical properties including thermal expansion (Ye et al. 2009), strength (Kavner 2003), seismic velocities (Jacobsen et al. 2004; Wang et al. 2003), and electrical conductivity (Yoshino et al. 2008; Huang et al. 2005; Poe et al. 2010).

Hydrogen incorporation in wadsleyite is dominated by a Mg vacancy charge-balanced with two hydrogen atoms, which can be described using Kröger-Vink notation (Kröger and Vink 1956) as $V_{Mg}^{''}+2(H^{\bullet})$. This substitution mechanism is generally accepted from a combination of crystal structure refinement (Smyth et al. 1997), IR spectroscopy (Jacobsen et al. 2005), and compositional systematics, in which d(Mg/Si)/d(H/Si)=-1/2 (Inoue et al. 1995). Hydrogen in wadsleyite appears to substitute as $V_{Mg}^{''}+2(H^{\bullet})$ principally at M3 in iron-free samples (Ye et al. 2010), while possibly additional mechanisms are active in iron-bearing systems (Kohlstedt et al. 1996).

Ringwoodite, however, does not follow the same compositional trend as wadsleyite, with d(Mg/Si)/d(H/Si)>-1/2, indicating additional substitution mechanisms that do not involve vacancies on the 16d site (Ohtani et al. 2000). FTIR spectra show a broad (~300 cm^{-1} HWHM) OH absorption band centered at ~3120 cm^{-1}, with some reports of overlapping bands at 3695 cm^{-1}, 3345 cm^{-1} (Kudoh et al. 2000; Smyth et al.

2003), 3220 cm^{-1} (Kohlsedt et al. 1996) and 2455 cm^{-1} (Bolfan-Casanova et al. 2000; Chamorro Pérez et al. 2006). Variations in the occurrence and frequencies appear correlated to the concentration of hydrogen and iron in the samples, but with broad consistency among spectra. Through correlation between the O-O distance and stretching frequency (e.g., Nakamoto et al. 1955; Libowitzky 1999), frequencies can be typically assigned to structural hydroxyls. These bands have been variably assigned to hydroxyls along the tetrahedral edge in a hydrogarnet-like defect (Smyth et al. 2003; Chamorro Pérez et al. 2006), substituting for the magnesium site (Kudoh et al. 2000; Smyth et al. 2003), or in the normally vacant octahedral site (16c) coupled with a Mg atom replacing a tetrahedral Si atom ($Mg_{Si}^{''}$) (Kudoh et al. 2000). Ambiguity in the interpretation is in large part a result of the broad OH band.

^{29}Si NMR- CPMAS spectra (Stebbins et al. 2009) of ringwoodite containing 1.0(1) wt% H_2O find that 4(2)% of the silicon is directly associated with hydrogen (as a Si-OH bond), consistent with a $V_{Mg}^{''}+2(H^{\bullet})$ defect mechanism accounting for about 25(12)% of the total OH, leading to the conclusion that the rest of the water incorporation is through additional mechanisms. Stebbins et al. (2009) also report no evidence of octahedral Si upon quench to 300 K with a detection level of about 0.5% of total Si present, suggesting no $Mg_{Si}''+2(H^{\bullet})$ defect mechanism active at 1.0(1) wt% H_2O.

First-principles calculations support a statistical distribution of hydrogen across multiple sites with a variety of substitution mechanisms (Panero 2010; Blanchard et al. 2009; Li et al. 2009), yet disagree with many of the interpretations from FTIR either in the relative proportions, frequency assignments, and hydrogen dynamics.

Absorption band broadening in OH vibrational frequencies can arise from a variety of sources. A statistical distribution across multiple sites will produce overlapping bands that are expected to narrow with decreasing temperature, and therefore vibrational spectroscopy at much lower temperatures may resolve these features and allow for more definitive assignment of the hydration mechanisms. The broad absorption peak can also be a result of fluid inclusions or disordered hydrogen along grain boundaries and line defects (e.g., Keppler and Rauch 2000). Bolfan-Casanova et al. (2000) showed that the FTIR spectrum of ringwoodite with 0.14 wt% H_2O does not change dramatically down to 223 K indicating that it is likely not due to fluid inclusions, which would freeze at those conditions. Alternatively, the broad OH absorption can result from either static or dynamic hydrogen disorder similar to that found in a glass or from the mobility of hydrogen on the time scale of the measurement.

We present the results of an FTIR study from 5 K to room temperature on three samples, two iron-free samples with 1.0(1) wt% H_2O and 2.5(3) wt% H_2O, and a Fo_{90} sample with 0.79 wt% H_2O (Table 1) to distinguish between static distribution amongst multiple sites of overlapping frequencies, or disordered hydrogen in the ringwoodite structure.

Methods

Sample Synthesis

Three samples were synthesized from oxides or synthetic ^{29}Si forsterite with brucite in the 5000-ton multi-anvil apparatus at Bayerisches Geoinstitut. Each sample was compressed to 20 GPa and heated to 1573-1673 K for 1-3 hours. Details of synthesis and characterization of Samples SZ0820, SZ0817 and SZ0002 are found in Ye et al.

(2012), Stebbins et al. (2009), and Smyth et al. (2003), respectively (Table 1). Sample SZ0817 was made from a $Mg_2{}^{29}SiO_4$ starting material and has been fully characterized by ^{29}Si MAS-NMR spectroscopy (Stebbins et al. 2009). SZ0820 has small amounts of excess stishovite evident under cross-polarized light, and SZ0817 showed trace superhydrous B in the NMR spectra (Stebbins et al. 2009) that is not evident through optical inspection.

Sample Polishing

Single crystals were selected for optical clarity and absence of inclusions. They were mounted in Loctite 366 UV adhesive on frosted slides and hand polished on one side using 3M-brand 3 μm diamond lapping film. Crystals were removed from the Loctite using an acetone solvent and recemented polished-side-down using Loctite or super-glue. Crystals were then ground and hand-polished using the same procedure to 20-72 μm thick as measured using a Mitutoyo ID-F125E digital micrometer.

Data Collection

All data were collected at the U2A beamline of the National Synchrotron Light Source (NSLS) using a synchrotron IR beam. Data were collected on the custom long-working distance microscope with a beam aperture of ~30 μm, and either a quartz or a KBr beamsplitter and an MCT detector. All spectra were collected with 512 or 1024 scans with 4 cm^{-1} spectral resolution. Operating at $<10^{-6}$ torr, the cryostat was cooled with liquid helium in 50 K steps. Temperature stability and accuracy of the temperature controller is <0.1 K at T> 50 K; ~0.5 K for T<20 K. Due to the polished and parallel surfaces of the samples, some of the spectra contained interference fringes, which were

118 removed via notch filtering of the Fourier transform of the transmission spectrum
119 consistent with sample thickness.

120 *Low-temperature FTIR measurements*

121 A fragment of each sample was pressed into a KBr pellet and mounted in a
122 modified Janis cryostat for measurements to low temperature at high-vacuum pressures
123 ($<10^{-6}$ torr). The samples were allowed to equilibrate at each temperature for at least 5
124 minutes before collecting data. Data were collected in two cooling cycles from room
125 temperature to ~11 K, the first using the quartz beamsplitter and the second with the KBr
126 beam splitter. No evidence of stishovite or superhydrous B was found in the infrared
127 spectra in any of the samples.

128 *Low-temperature, high-pressure FTIR measurements*

129 A polished, 25 μm thick sample SZ0820 (2.5(3) wt% H_2O from SIMS, iron-free)
130 was loaded with a ruby chip in a Ne pressure medium in a symmetric diamond cell with
131 type-IIa diamonds and compressed to 31 GPa. Cooling of the DAC was done in a CRYO
132 Industries cryostat model 102-2572-DCA cooled with liquid helium using Varian TPS-
133 compact vacuum system to ~10^{-6} torr. Upon cooling, the pressure in the cell increased to
134 35 GPa through thermal contraction on the apparatus. The R1 line of ruby shifts to
135 shorter wavelengths upon cooling, while the intensity of the R2 line decreases
136 dramatically below 40 K (Fig 1). A small ruby ball was therefore mounted on the back of
137 one of the diamonds to confirm that the cryostat thermal couple temperature, that is
138 located above the diamond cell, accurately reflects the temperature of the sample itself.

139 The high-pressure data were collected in two cooling cycles in 50 K steps to 5 K,
140 the first cooling cycle beginning at 31 GPa, and then again after decompression to 23

GPa. Additional spectra at room temperature were collected on the U2A sidestation upon decompression at 19, 15, 8, 3, and 0 GPa.

Superhydrous B was readily observed in the fragment of SZ0820 that was used at high pressure, yet superhydrous B was not otherwise evident in x-ray diffraction or optical inspection under cross-polarized light in different fragments of this sample. This is consistent with <1 vol% superhydrous B in the sample. Care was taken to avoid these regions, but minor superhydrous B is evident in some spectra throughout.

Results

High-vacuum FTIR Spectra

The high-vacuum ($<10^{-6}$ torr), room-temperature spectra of the three samples are all broadly similar to each other (Fig 2) and nearly identical as those described in Chamorro Pérez et al. (2006) and Bolfan Casanova et al. (2000) for all three samples. The iron-free sample with the 2.5(3) wt% H_2O (SZ0820) is dominated by an OH stretching band centered at 3122 cm^{-1} with a width (HWHM) of ~ 250 cm^{-1}. The iron-free sample with 1.0(1) wt% H_2O (SZ0817) has a lower central frequency at 3078 cm^{-1}, consistent with observations of frequency dependence as a function of water content (Chamorro Pérez et al. 2006). The sample with higher water content (SZ0820) has a distinct shoulder at ~3665 cm^{-1}, absent in the sample with lower water content (SZ0817). The Fo_{90} sample with 0.79 wt% H_2O (SZ0002) is very similar to the iron-free SZ0820 sample, with a high frequency shoulder and a main OH stretching frequency of 3147 cm^{-1} as previously reported (Smyth et al. 2003).

Upon cooling we observe no major changes are noted in the 1100-2400 cm^{-1} region for any of the samples at low temperatures except for moderate narrowing (~10%) of peaks with cooling and subsequent recovery of thermal broadening upon return to 300 K.

In the OH stretching region, a shoulder becomes evident at ~3265 cm^{-1} in the iron-bearing sample (SZ0002) below 50 K, not retained at room temperature (Fig 2b). No significant change is seen in the OH stretching region of SZ0820 (Fig 2b) with moderate narrowing of the main band and a slight increase in the absorption at 3100 cm^{-1} at 11 K, and a -3 cm^{-1} shift of the shoulder of to 3662 cm^{-1}.

We observe a distinct change upon cooling of the sample with lower water content, iron-free sample, SZ0817, with splitting of the main OH stretching peak (3127 cm^{-1}) to two peaks at 3088 and 3273 cm^{-1} at temperatures below 200 K (Fig 3). This splitting remains evident upon returning to room temperature and was seen throughout a second cooling cycle. This behavior is similar to the splitting observed in γ-Mg_2GeO_4 (Thomas et al. 2008), in which a broad 3207 cm^{-1} peak is resolved into two peaks at 3170 and 3240 cm^{-1} at <100 K. The authors, however, also report a series of sharper peaks at higher frequencies not seen here, arguing that the OH defect distribution is inherently different in the germanate than the silicate.

High-Pressure FTIR Spectra

At 31 GPa and room temperature, the IR spectra of sample SZ0820 are broadly consistent with previously published data (Chamorro Pérez et al. 2006) (Fig 4). The room-temperature pressure shift of the 1282 cm^{-1} band is 1.8 cm^{-1}/GPa, the same value reported in Chamorro Pérez et al. (2006), and therefore consistent with the interpretation

of an X-OH bending mode instead of an Si-O overtone. While the X-OH bands in the 1100-1600 cm^{-1} frequency window are all evident as assigned by Chamorro Pérez et al. (2006), interference and noise make the pressure dependence observed here difficult to discuss quantitatively. We observe additional bands of uncertain assignment resolved upon decompression at room temperature, evident from 31 GPa down to 8 GPa at 2451 and 2654 cm^{-1} (Fig 4). The 2654 cm^{-1} band is nearly invariant with pressure, while the 2451 cm^{-1} band increases at ~1 cm^{-1}/GPa.

We observe a similar loss of absorption at 35 GPa in the ringwoodite OH stretching region as observed in Chamorro Pérez et al. (2006) and Koch-Müller et al. (2011). Portions of the sample show clear OH absorption in superhydrous B inclusions at 3440 cm^{-1} and 3330 cm^{-1} at 35 GPa, with no significant narrowing (<5%) of the two OH bands in superhydrous B inclusions during the cooling cycle to 5 K. These superhydrous B OH absorption bands shift upon room-temperature decompression to 3444 and 3349 cm^{-1} at 23 GPa, then ultimately to 3406 cm^{-1} and 3349 cm^{-1} at 0 GPa, with $d\nu/dP$=0.97 cm^{-1}/GPa and -0.54 cm^{-1}/GPa, respectively, consistent with FTIR compression of superhydrous B to 15 GPa (Koch-Müller et al. 2005). At room temperature, the higher frequency OH absorption (3406 cm^{-1} at 0 GPa) has a HWHM of 55 and 65 cm^{-1} at 35 and 23 GPa, respectively, relaxing to 29 cm^{-1} at ambient pressure, which we interpret as the release of non-hydrostatic stress within the ringwoodite grain.

The ringwoodite sample, while loaded in neon, therefore exhibits some amount of internal deviatoric stress. It has been suggested that the loss of OH stretching absorption in ringwoodite above 20 GPa as observed here reflects the non-hydrostatic stress in the quasi-hydrostatic, solid rare gas pressure medium (Koch-Müller et al. 2011), not proton

disorder in the spinel structure as a result of potential well broadening with the shortening of the O-O distances (Chamorro Pérez et al. 2006).

Upon room-temperature decompression to 23 GPa we do not see the return of OH stretching absorption at room temperature, but it does return upon cooling to 5 K at 3178 cm^{-1}, and it is then retained at room temperature and at all pressures below 23 GPa (Fig 4).

Below 23 GPa as many as 4 additional bands become evident (3471, 3252, 3041, and 2841 cm^{-1}), and at 8 GPa, the lowest pressure where three of the bands remain evident, the frequencies are 3281, 3038, and 2831 cm^{-1}, respectively, for $d\nu/dP$=-1.9, +0.2, and -0.67 cm^{-1}/GPa for the three traceable peaks. The change in frequency for the central maximum at 31 GPa compared to ambient pressure is -11.1 cm^{-1}/GPa (-8 cm^{-1}/GPa average slope between 0 and 19 GPa), while the low frequency band decreases from 2863 cm^{-1} at 3 GPa to 2823 cm^{-1} at 31 GPa with $d\nu/dP$=-0.9 cm^{-1}/GPa. The 3281 cm^{-1} band appears consistent with the shoulder evident in SZ0002 and the resolved peak in SZ0817 at high-vacuum pressures and low temperature with $d\nu/dP$=-1.9 cm^{-1}/GPa. These other observed bands may simply be the artifact of internal reflections between the diamond faces or the top and bottom of the polished ringwoodite grain itself. Each spectrum has been notch filtered to remove such effects, with minimal, but persistent fringes remaining evident in the 4000-6000cm^{-1} range for 3-23 GPa (Fig 4). The fringe spacing ($\Delta\nu/<\nu>$) does not change consistently with the change in pressure (0.065 at 23 GPa; 0.077 at 8 GPa), nor is the spacing consistent in the 4000-6000 cm^{-1} region, where the spacing is 0.10 regardless of pressure. Nevertheless, we proceed with caution in

assignment of these peaks recognizing that this may instead be an artifact of internal reflections.

Discussion and conclusions

Interpretation of Defect Mechanisms

Both low temperature and high pressure were required to separate multiple overlapping absorption bands, reflecting a multiplicity of OH bonding environments. The observed splitting of peaks, when compared to the crystal structure and proposed defect mechanisms is therefore consistent with the population model of Panero (2010). In the hydrous samples, the lower energy defect mechanisms are preferentially populated in the samples containing less water: populating those sites along the octahedral edges first through the $V_{Mg}^{''}+2(H^{\bullet})$ defect mechanism, then the hydrogarnet mechanism ($V_{Si}^{''''}+4(H^{\bullet})$), followed finally by the $Mg_{Si}^{''}+2(H^{\bullet})$ mechanism. The high-vacuum, room-temperature ~3100 cm^{-1} band therefore represents an overlapping of OH stretching modes for hydrogen bonded along octahedral edges either along the edges of the Mg vacancies (16d site) or the nominally vacant 16c site associated with the Mg vacancy at ~3100 cm^{-1} and ~3270 cm^{-1}, where the frequency is a function of the OH content, reflecting the positive volume of hydration expanding the crystal lattice. This is observed in all three samples, indicating similar population mechanism in each. The iron-bearing sample and the sample with greatest water content, also make use of the $V_{Si}^{''''}+4(H^{\bullet})$ defect mechanism as seen at ~3650 cm^{-1}, and reflecting the volume expansion of the Si site consistent with hydrogarnet defects (e.g., Lager and Von Dreele 1996). Finally, the

254 $Mg_{Si}^{''}+2(H^{\bullet})$ defect mechanism is in the lowest proportions and seen at the low
255 frequency end of ~2800 cm^{-1} observed at low temperature and high pressure.

256 The 2654 cm^{-1} band is nearly invariant with pressure, while the 2451 cm^{-1} band
257 increases at ~1 cm^{-1}/GPa. Chamorro Pérez et al. (2006) interpret these as overtones of in-
258 or out-of-plane X-OH bending, yet the small frequency shifts with pressure may dispute
259 this interpretation, which would predict a large and positive slope. This behavior is also
260 inconsistent with a strong hydrogen bond as would be predicted if this were OH
261 stretching. Such a low frequency would predict a O-O distance of ~2.6 Å (Libowitzky
262 1999). The 8a site has a short O-O bond distance (2.36 Å at 0 GPa) and long OH bond
263 lengths (1.11 Å) (Panero 2010) suggesting hydrogen associated with a substitution in the
264 nominally vacant 16c site in the $V_{Mg}^{''}+2(H^{\bullet})$.

265 Two bands, at 1286 and 1352 cm^{-1} (frequencies for SZ0820), are assigned as in-
266 plane bending of X-OH by Chamorro Pérez et al. (2006). The area under each band in
267 SZ0820 is about 1.4 times that in the SZ0817 (Fig 2a) consistent with these X-OH bands
268 populated first. In contrast, the band at 1176 cm^{-1} (assigned as out-of-plane X-OH
269 bending) is more than 10 times the absorbance in SZ0820. Therefore, we interpret the
270 1286 and 1352 cm^{-1} in-plane bending of X-OH as Si-OH bending reflecting the OH
271 bonding in the $V_{Mg}^{''}+2(H^{\bullet})$ defect mechanism with hydrogen either bonded along the
272 nominally vacant 16d octahedral edge of the $V_{Mg}^{''}$ 16c octahedral edge. In contrast, the
273 1176 cm^{-1} band is interpreted here as $Mg_{Si}^{''}$-OH out-of-plane bending, not populated until
274 high OH contents.

275 The overlapping of these bands is interpreted here as a statistical distribution
276 across multiple bonding sites with similar O-O distances in the high-symmetry spinel

277 structure, compounded by the width of the absorption band resulting from nearly free
278 rotation of the bent hydrogen bonds, consistent with the bond distribution in Panero
279 (2010). This conclusion that the effects of low temperatures and compression serve to
280 more directly isolate each bonding site is consistent with the more complex FTIR spectra
281 in which hydrous ringwoodite is synthesized after annealing in the wadsleyite field
282 (Kohlstedt et al. 1996), which also likely contributed to annealing of hydrogen positions
283 into distinct lower energy sites.

284 *Geophysical Implications*

285 The majority of hydrogen in ringwoodite is very loosely bound to the structure,
286 taking on a multitude of bonding sites with a nearly continuous distribution of OH..O
287 bond distances. The most tightly bound hydrogen sites are populated first (<1% H_2O),
288 resulting in the splitting observed below 150 K (kT<0.013 eV), a fraction of the thermal
289 energy of the ~1 eV activation energy for proton conductivity in ringwoodite (Yoshino et
290 al. 2008; Huang et al. 2005) but comparable to the activation energy of rotational
291 diffusion of protonic defects which are on the order of tens of meV (e.g., Kreuer 1999).
292 The shoulder evident at lower temperatures in the samples with higher water content
293 indicate that these OH bonds have the shortest OH..O distances, and therefore consistent
294 with the hydrogarnet substitution.

295 The broad, overlapping OH bands are likely more representative of the
296 distribution of hydrogen in the high-pressure, high-temperature conditions of the Earth's
297 transition zone, however. Under these conditions, the disorder of hydrogen within and
298 between sites predicts a higher mobility of hydrogen within the structure.

The FTIR spectrum of ringwoodite is distinctly different than in wadsleyite, which is otherwise structurally similar with alternating OT and O layers through the structure. Both structures are based on a cubic-close-packed oxygen sublattice, but wadsleyite is a sorosilicate with Si_2O_7 groups, one bridging oxygen (O2), and one non-silicate oxygen (O1). However, wadsleyite appears to incorporate hydrogen through a much more limited number of mechanisms, namely the $V_{Mg}^{''}+2(H^{\bullet})$ defect at M3 with protonation primarily of the non-silicate oxygen (Smyth et al. 1997; Kudoh et al. 2000; Tsuchiya and Tsuchiya 2009; Ye et al. 2010). This leads to a relatively simple FTIR spectrum with 3-4 absorption bands each with FWHM widths <100 cm^{-1} that does not change in character over two orders of magnitude of water content (Jacobsen et al. 2005; Jacobsen 2006).

The contrasts in the way in which water is incorporated in each of these post-olivine structures predicts that they may be geophysically observable between the top and bottom of the Earth's transition zone as a function of water content. The greatest effect would be in the electrical (proton) conductivity differences of these two materials, but also differences in the rate of change of elastic properties with increasing water contents. The measurement and interpretation of electrical conductivity data is difficult, with debate on the consequences of dehydration, grain boundary, iron redox state, and measurement method.

There is significant debate as to the electrical conductivity of ringwoodite and wadsleyite as a function of water and iron content, where charge can be transferred through protons as well as polaron conduction, or the hopping of electrons between Fe^{2+} and Fe^{3+}. The iron-independent conductivity has alternately been be expressed as

$$\sigma_c = AC_W^r \exp\left(-\frac{H}{RT}\right) \quad (1)$$

or

$$\sigma_c = \sigma_{0c} \exp\left(-\frac{H - \alpha C_W^{1/3}}{kT}\right) \quad (2)$$

by Huang et al. (2005) and Yoshino et al. (2008), respectively, where σ_C is the conductivity, A is a scaling factor (S/m) and C_w is the concentration of water (wt%). H is an aggregate activation enthalpy potentially encompassing multiple mechanisms, k is the Boltzmann's constant, and T is temperature in Kelvin. The exponent r reflects non-linear effects of water in the crystal as a consequence of multiple hydrogen atoms in a single defect (e.g. $(2H)_{Mg}^{X}$) and assumes a single migration mechanism with variable water contents (Eq. 1) (Huang et al. 2005), while the coefficient α reflects the activation energy dependence resulting from more closely spaced defects. The functional form employed by Yoshino et al. (2008) (Eq. 2) reflects variable charge mobility as a function of water content. This second model is supported by the interpretation here with sequential population of sites.

Despite the uncertainty in the absolute value, migration enthalpy, or even functional form of conductivity, the electrical conductivity of hydrous ringwoodite is consistently found to be greater than hydrous wadsleyite for comparable water contents, experimental conditions, and measurement technique. For example, at 1500 K, Huang et al. (2005) measured the proton conductivity of ringwoodite containing 1 wt% H_2O to be about three times greater than wadsleyite with 1 wt% H_2O (0.96 vs 0.33 S m^{-1}), while Yoshino et al. (2008) report values to be 22 times greater (0.87 vs 0.04 S m^{-1}). Yoshino et al. (2008) show a dramatic rise in the proton conductivity of ringwoodite relative to

wadsleyite with increasing water content. These observations then support the interpretation that given the multiplicity of hydrogen defect mechanisms in ringwoodite, hydrogen is loosely bound in the structure, particularly for water contents >0.5 wt% H_2O. The proton conductivity is significantly higher in ringwoodite than in wadsleyite (Yoshino et al. 2008), where the apparent activation enthalpy for proton migration decreases from 1.1 eV to 0.5 eV is a function of the dominant hydrogen configuration with increasing water content, in which most of the decrease happening in the first 0.5 wt% H_2O.

This conclusion has direct implications on the interpretation of the transition zone, where the presence of or variations in hydrogen content has been implicated as having a large effect on the electrical conductivity of the mantle. While the appropriate interpretation of these measurements as a function of oxygen fugacity and the presence of other minerals is not settled (Huang et al. 2005; Hirschmann 2006), the incorporation mechanism of hydrogen in ringwoodite places an additional bound, predicting a variable behavior with increasing water content.

Acknowledgements

This work was supported by NSF EAR 09-55647 to WRP and NSF EAR 07-11165 and EAR 11-13369 to JRS. Thanks to Tao Zhou for the loan of the Janis cryostat. The use of the U2A beamline at the National Synchrotron Light Source beamline is supported by COMPRES, the Consortium for Materials Properties Research in Earth Sciences under NSF Cooperative Agreement EAR 06-49658 and by the U.S. Department of Energy, Office of Science, Office of Basic Energy Sciences, under Contract No. DE-AC02-

98CH10886. This manuscript was greatly improved by comments from S. Demouchy, R. Stalder, and an anonymous reviewer.

References

Blanchard, M., Balan, E., and Wright, K. (2009) Incorporation of water in iron-free ringwoodite: A first-principles study. American Mineralogist, 94, 83-89.

Bolfan-Casanova, N., Keppler, H., and Rubie, D.C. (2000) Water partitioning between nominally anhydrous minerals in the MgO-SiO_2-H_2O system up to 24 GPa: implications for the distribution of water in the Earth's mantle. Earth and Planetary Science Letters, 182, 209-221.

Chamorro Pérez, E.M., Daniel, I., Chervin, J.-C., Dumas, P., Bass, J.D., and Inoue, T. (2006) Synchrotron IR study of hydrous ringwoodite up to 30 GPa. Physics and Chemistry of Minerals, 33, 502-510.

Demouchy, S., Deloule, E., Frost, D.J., and Keppler, H. (2005) Pressure and temperature-dependence of water solubility in iron-free wadsleyite. American Mineralogist, 90, 1084-1091.

Hirschmann, M. (2006) Earth Science: A Wet Mantle Conductor?. Nature, 439, E3.

Huang, X.G., Xu, Y.S., and Karato, S.I. (2005) Water content in the transition zone from electrical conductivity of wadsleyite and ringwoodite. Nature, 434, 746-749.

Inoue, T., Yurimoto, H., and Kudoh, Y. (1995) Hydrous modified spinel, $Mg_{1.75}SiH_{0.5}O_4$: a new water reservoir in the mantle transition region. Geophysical Research Letters, 22, 117-120.

Jacobsen, S.D. (2006) Effect of water on the equation of state of nominally anhydrous minerals. Reviews in Mineralogy and Geochemistry, 62, 321-342.

Jacobsen, S.D., Smyth, J.R., Spetzler, H., Holl, C.M., and Frost, D.J. (2004) Sound velocities and elastic constants of iron-bearing hydrous ringwoodite. Physics of the Earth and Planetary Interiors, 143-144, 47-56.

Jacobsen, S.D., Demouchy, S., Frost, D.J., and Boffa-Ballaran, T. (2005) A systematic study of OH in hydrous wadsleyite from polarized spectroscopy and single-crystal X-ray diffraction: oxygen sites for hydrogen storage in Earth's interior. American Mineralogist, 90, 61-70.

Kavner, A. (2003) Elasticity and strength of hydrous ringwoodite at high pressure. Earth and Planetary Science Letters, 214, 645-654.

Keppler, H. and Rauch, M. (2000) Water solubility in nominally anhydrous minerals measured by FTIR and 1H MAS NMR: the effect of sample preparation. Physics and Chemistry of Minerals, 27, 371-376.

Koch-Müller, M., Dera, P., Fei, Y., Hellwig, H., Liu, Z., Van Orman, J., and Wirth, R. (2005) Polymorphic phase transition in superhydrous phase B. Physics and Chemistry of Minerals, 32, 349-361.

Koch-Müller, M., Speziale, S., Deon, F., Mrosko, M., and Schade, U. (2011) Stress-induced proton disorder in hydrous ringwoodite. Physics and Chemistry of Minerals, 38, 65-73.

Kohlstedt, D.L., Keppler, H., and Rubie, D.C. (1996) Solubility of water in the alpha, beta and gamma phases of $(Mg,Fe)_2SiO_4$. Contributions to Mineralogy and Petrology, 123, 345-357.

Kreuer, K.D. (1999) Aspects of the formation and mobility of protonic charge carriers and the stability of perovskite-type oxides. Solid State Ionics, 125, 285-302.

Kröger, F.A. and Vink, H.J. (1956) Relation Between the Concentrations of Imperfections in Crystalline Solids. Academy Press, New York.

Kudoh, Y., Kuribayashi, T., Mizobata, H., and Ohtani, E. (2000), Structure and cation disorder of hydrous ringwoodite, γ-$Mg_{1.89}Si_{0.98}H_{0.30}O_4$. Physics and Chemistry of Minerals, 27, 474-479.

Lager, G.A. and Von Dreele, R.B. (1996) Neutron powder diffraction study of hydrogarnet to 9.0 GPa. American Mineralogist, 81, 1097-1104.

Li, L., Brodholt, J., and Alfe, D. (2009) Structure and elasticity of hydrous ringwoodite: A first principles investigation. Physics of the Earth and Planetary Interiors, 177, 103-115.

Libowitzky, E. (1999) Correlation of O-H Stretching Frequencies and O-H…O hydrogen bond lengths in minerals. Monatshefte für Chemie, 130, 1047-1059.

Nakamoto, K., Margoshes, M., and Rundle, R.E. (1955) Stretching frequencies as a function of distances in hydrogen bonds. Journal of the American Chemical Society, 77, 6480-6486.

Ohtani, E., Mizobata, H., and Yurimoto, H. (2000) Stability of dense hydrous magnesium silicate phases in the systems Mg_2SiO_4-H_2O and $MgSiO_3$-H_2O at pressures up to 27 GPa. Physics and Chemistry of Minerals, 27, 533-544.

Panero, W.R. (2010) First-principles determination of the structure and elasticity of hydrous ringwoodite. Journal of Geophysical Research, 115, B03203.

Poe, B.T., Romano, C., Nestola, F. and Smyth, J. R. (2010) Electrical conductivity anisotropy of hydrous olivine. Physics of the Earth and Planetary Interiors, 181, 103-111.

Smyth, J.R., Kawamoto, T., Jacobsen, S.D., Swope, R.J., Hervig, R.L., and Holloway,

J.R. (1997) Crystal structure of monoclinic hydrous wadsleyite. American Mineralogist, 82, 270-275.

Smyth, J.R., Holl, C.M., Frost, D.J., Jacobsen, S.D., Langenhorst, F., and McCammon, C.A. (2003) Structural systematics of hydrous ringwoodite and water in Earth's interior. American Mineralogist, 88, 1402-1407.

Stebbins, J.F., Smyth, J.R., Panero, W.R., and Frost, D.J. (2009) Forsterite, hydrous and anhydrous wadsleyite and ringwoodite (Mg_2SiO_4): ^{29}Si NMR results for chemical shift anisotropy, spin-lattice relaxation, and mechanism of hydration. American Mineralogist, 94, 905-915.

Tsuchiya, J. and Tsuchiya, T. (2009) First principles investigation of the structural and elastic properties of hydrous wadsleyite under pressure. Journal of Geophysical Research, 114, B02206.

Thomas, S.M., Koch-Mueller, M., Kahlenberg, V., Thomas, R., Rhede, D., Wirth, R., and Wunder, B. (2008) Protonation in germanium equivalents of ringwoodite, anhydrous phase B, and superhydrous phase B. American Mineralogist, 93, 1282-1294.

Wang, J., Sinogeikin, S.V., Inoue, T., and Bass, J.D. (2003) Elastic properties of hydrous ringwoodite. American Mineralogist, 88, 1608-1611.

Ye, Y., Schwering, R.A., and Smyth, J.R. (2009) Effects of hydration on thermal expansion of forsterite, wadsleyite, and ringwoodite at ambient pressure. American Mineralogist, 94, 899-904.

Ye, Y., Smyth, J.R., Hushur, A., Lonappan, D., Manghnani, M.H., Dera, P., and Frost, D.J. (2010) Crystal structure of hydrous wadsleyite with 2.8% H_2O and compressibility to 60 GPa. American Mineralogist, 95, 1765-1772.

Ye. Y., Brown, D.A., Smyth, J.R., Panero, W.R., Jacobsen, S.D., Chang, Y.Y., Townsend, J.P., Thomas, S.M., Hauri, E.H., Dera, P., and Frost, D.J. (2012) Compressibility and thermal expansion of hydrous ringwoodite with 2.5(3) wt% H_2O. American Mineralogist, 97, 573-582.

Yoshino, T., Manthilake, G., Matsuzaki, T., and Katsura, T. (2008) Dry mantle transition zone inferred from the conductivity of wadsleyite and ringwoodite. Nature, 451, 326-329.

471 Table 1: Samples and experimental conditions

	Mg#	Synthesis P (GPa)	Synthesis T (K)	Other phases present	wt% H_2O	FTIR Measurements		
						Thickness (μm)	Pressure (GPa)	Temperature
SZ0820 Ye et al. 2012	100	20	1523	Stishovite & Super-hydrous B	2.5(3) (SIMS) 1.6 (FTIR)	25	35 GPa 23 GPa	300 K to 5 K in 50 K steps
							Decompression from 23 GPa	300 K
						60	0 GPa	300 K to 11 K in 50 K steps
SZ0002 Smyth et al. 2003	91	20	1673	None evident	0.79 (FTIR)	72	0 GPa	300 K to 11 K in 50 K steps
SZ0817 Stebbins et al. 2009	100	20	1573	Super-hydrous B	1.0(1) (FTIR)	20	0 GPa	300 K to 11 K in 50 K steps

472

473

Figure 1. The R1 peak position of a ruby ball on the thermocouple within the cryostat upon cooling (open circles) and warming (closed circles), compared to data collected from a ruby ball placed on the back of the DAC containing the ringwoodite sample (open diamonds). Inset shows the ratio of the R2 to the R1 peak intensity as a function of temperature below 40 K.

Figure 2. Spectra of each sample (SZ0820, black, SZ0002, blue, SZ0817 red) normalized to 100 μm thickness for the X-OH bending region (a) and OH stretching (b). Curves are shifted vertically for clarity. Labels reflect the frequencies at low temperature (thick lines) with no significant shift observed at room temperature (thin lines) before (dashed) and after temperature cycling (solid). Sample 817 demonstrates narrowing and splitting of peaks upon cooling, without significant additional peaks. Stars (*) indicate residual Loctite on the sample as well as C-H on the synchrotron mirrors.

Figure 3. OH absorption of sample SZ0817 with decreasing temperature on first cooling cycle showing the development of a new peak at ~3260 cm^{-1} as the 3100 cm^{-1} peak narrows with cooling. The process is reproducible with a second cooling cycle. Stars (*) indicate residual Loctite on the sample as well as C-H on the synchrotron mirrors. Curves are offset vertically for clarity.

Figure 4. Selected infrared absorption specta of sample SZ0820 at from 35 GPa to ambient, at room temperature (thin lines) and 5 K (thick lines). The distinct OH peaks evident below 23 GPa merge below 8 GPa to recover the pre-compression, pre-cooling spectrum.

Figures

Figure 1

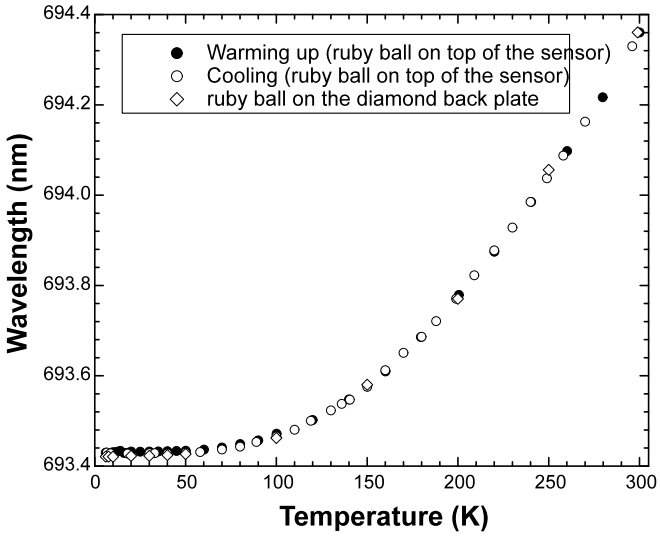

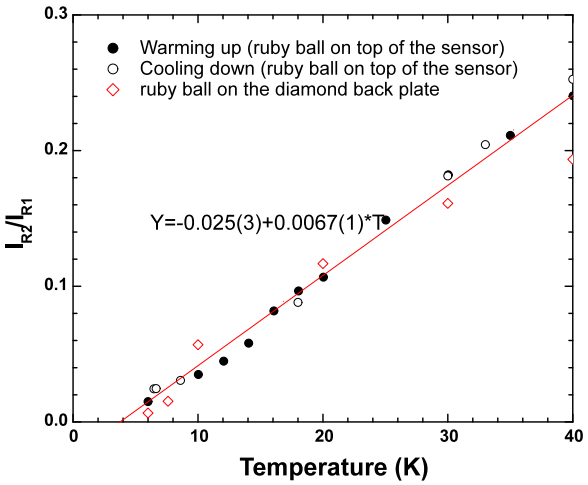

Figure 2

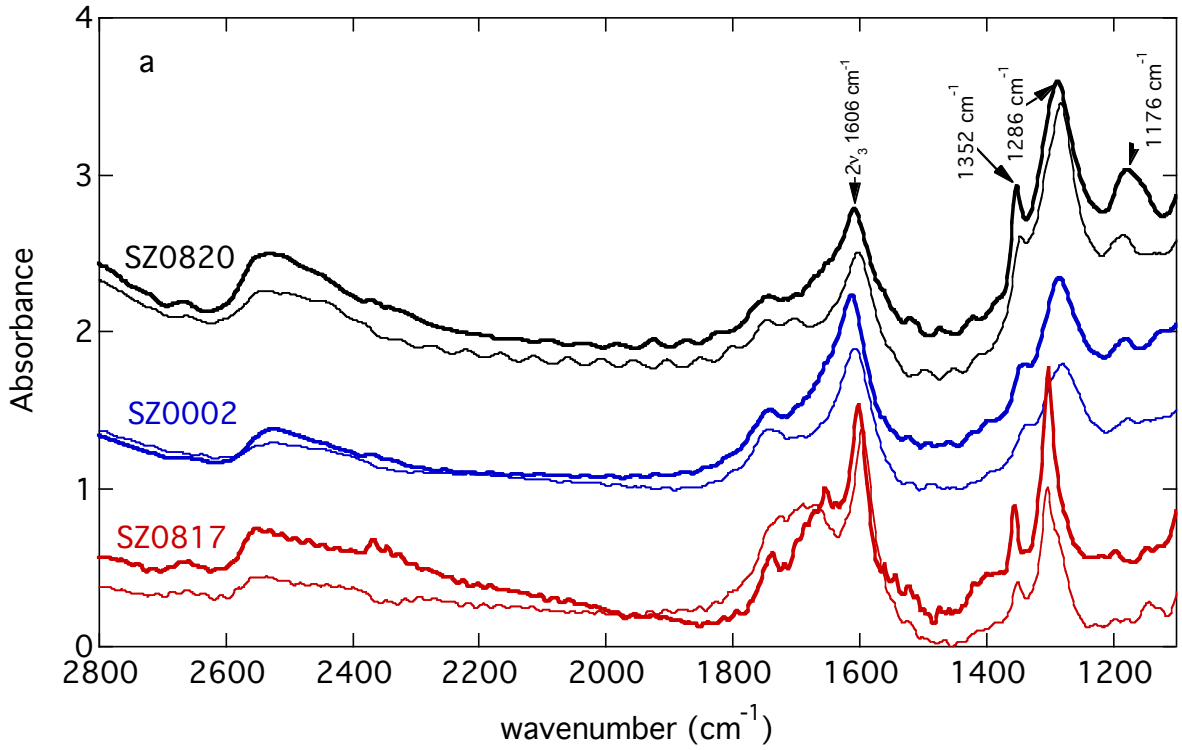

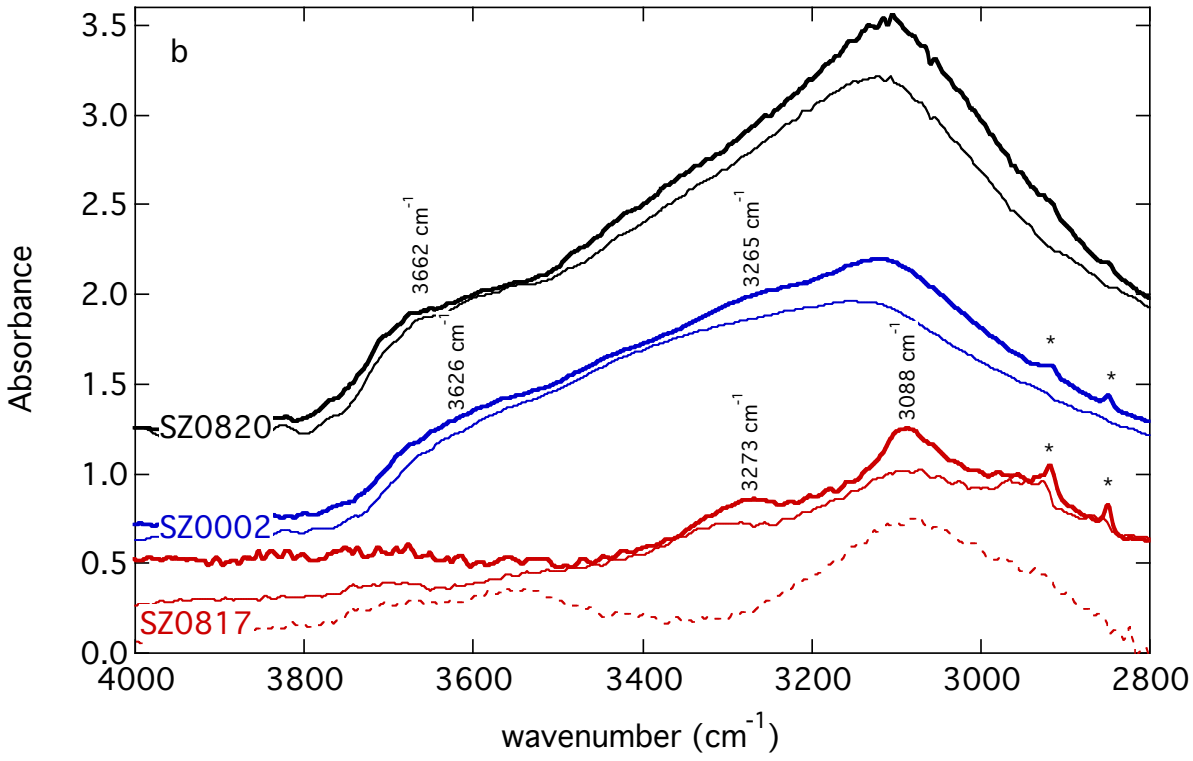

Figure 3

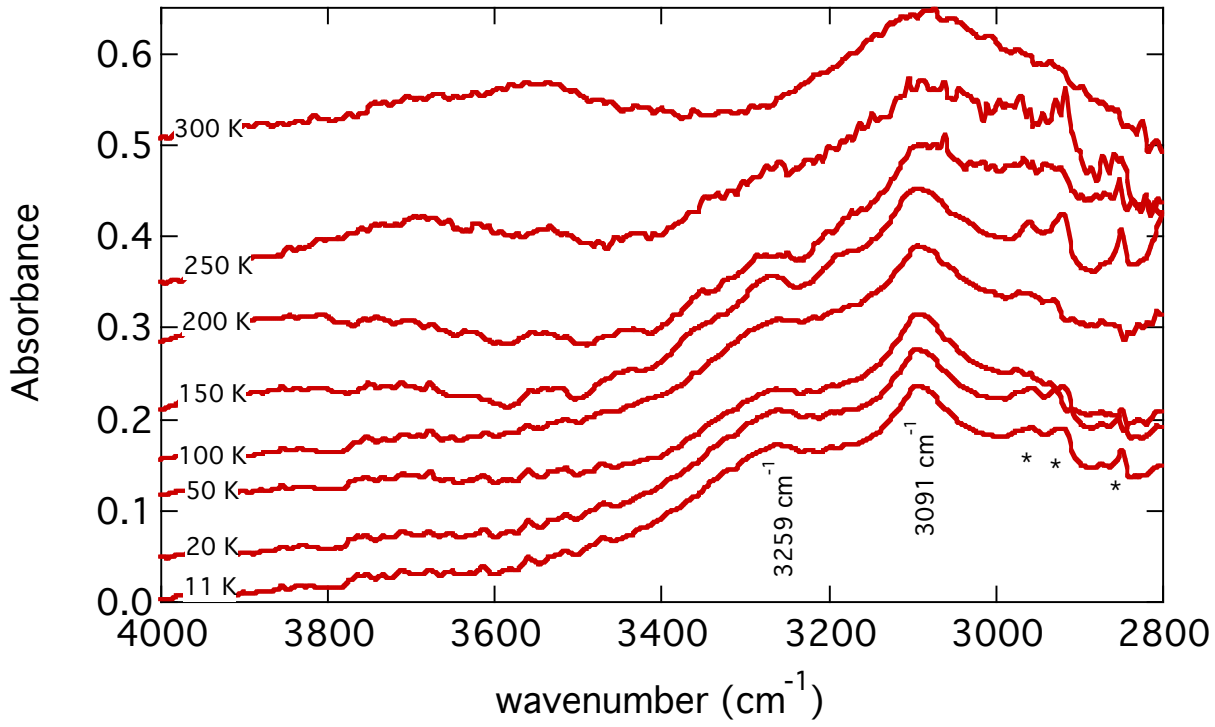

Figure 4